Analysis, design, and optimization of structures with integral compliant mechanisms for mid-frequency response

Ercan M. Dede*,[†],[‡] and Gregory M. Hulbert[§]

Department of Mechanical Engineering, University of Michigan, Ann Arbor, MI 48109-2125, U.S.A.

SUMMARY

A multi-scale paradigm is proposed that utilizes periodic, small-scale, integral compliant mechanisms within larger-scale structures for the attenuation of vibro-acoustic response. Amplification principles serve as the basis for the design of these mechanisms in achieving reduced energy transmission. The spectral finite element method is exploited for a force–velocity and energy flow analysis of the resultant truss-like structures. A genetic algorithm is employed to optimize structure size for greatest effectiveness in the frequency range of interest. This study demonstrates that a significant decrease in structural vibration is achievable and suggests promising applications including the design of acoustic isolation panels for broadband vehicle noise reduction. Copyright © 2007 John Wiley & Sons, Ltd.

1. INTRODUCTION

The vibration of lightweight structures in the 1–10 kHz middle frequency region generates noise, which has an adverse effect on human performance and perception of quality [1–5]. Typical solutions, such as spring–mass absorbers, visco-elastic coatings, and active control, are effective across these frequencies. Nonetheless, they often lead to greater system complexity or weight [6, 7]. Accordingly, the objective of this work is to introduce a new technique for the reduction of middle frequency structural-borne noise.

---

*Correspondence to: Ercan M. Dede, Department of Mechanical Engineering, University of Michigan, 2250 G.G. Brown, 2350 Hayward, Ann Arbor, MI 48109-2125, U.S.A.
[†]E-mail: dedeem@umich.edu
[‡]Doctoral Candidate.
[§]Professor.

WILEY
InterScience®
DISCOVER SOMETHING GREAT

Much work has been performed over the last century in order to understand the basic principles of wave propagation in periodic lattices and structures [8–10]. Structures with *band gap* characteristics have been identified and have become the subject of recent investigation [11–16]. Such structures have frequency bands in which wave propagation is either hindered (i.e. *stop bands*) or unhindered (i.e. *pass bands*). The ability to control the location and range of stop bands, also known as response attenuation zones, has garnered further interest specific to the vibration of and sound radiation from sandwich beams made with periodic truss cores [17, 18]. The traditional square core, as well as 'reentrant' or negative Poisson ratio core topologies have been examined. From this prior work it is well established that as frequency of vibration increases, wavelength decreases, producing localized deformations in structures. In view of this, a methodology is introduced herein, which encompasses integrated, designed, small-scale compliance to achieve noise reduction.

To reduce middle frequency response, the principle of mechanical advantage is exploited as a design tool to limit energy transmission. In this paper, a novel use of compliant mechanisms is followed to attain the mechanical advantage. From the computational standpoint, an efficient spectral finite element approach is employed in order to accurately predict the structural dynamic response and reduce the size of the analysis [19]. The output of this analysis includes basic velocity and energy flow information to provide insight into the performance of the structures. A genetic algorithm capable of optimizing truss-like structures that have a large number of non-linear, inter-related variables is then brought forth to supplement the initial design process [20, 21].

The paper is organized as follows: in Section 2, a brief review of the spectral finite element method is given. Then, the analysis and design of a compliant mechanism unit cell and structure is introduced in Section 3. Genetic algorithm optimization of the compliant mechanism unit cell is presented in Section 4. Finally, conclusions are drawn in Section 5 along with directions of future effort including prototype testing for model validation.

2. THE SPECTRAL FINITE ELEMENT METHOD—REVIEW

This section provides a brief review of the spectral finite element method. A comprehensive development of the dynamic stiffness matrix for both the rod and the beam element, along with background details on the formulation of the method, can be found in [19].

Consider a general linear frame element that combines the degrees of freedom of both a rod element and a beam element, shown in Figure 1. The element material density, Young's modulus, cross-sectional area, length, and area moment of inertia are denoted by ρ, E, A, L,
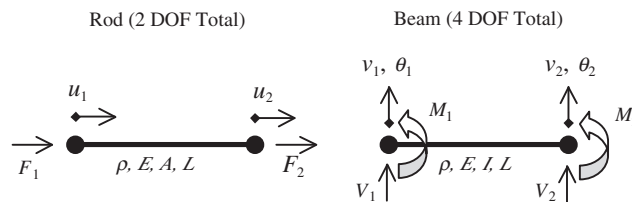

Figure 1. Rod and beam element nodal degrees of freedom and loads.

and I, respectively. The rod element axial loads and displacements are specified, respectively, by F_i and u_i, while the beam transverse loads, moments, transverse displacements, and rotations are given, respectively, by V_i, M_i, v_i, and θ_i, where i denotes the node number of interest.

2.1. Rod element formulation

In the development of a spectral rod element, the mass is not lumped at the ends of the element as is often done with a conventional finite element formulation [22]. Rather, the mass is considered distributed evenly along the length, which allows for the propagation of longitudinal waves through the element, acting as a waveguide. It has been established that the space–time solution for the longitudinal displacement of a point on the rod can be represented by

$$u(x, t) = \sum_n \hat{u}_n(x, \omega_n) \mathrm{e}^{\mathrm{i}\omega_n t} \tag{1}$$

In fact, (1) represents the general solution for the time harmonic variation of any variable, where ω is the frequency and (1) is summed over the number of frequencies of interest, n. In this equation, the ˆ nomenclature is established to represent a spectral quantity. Thus, the spectral displacements for the rod element are represented by $\hat{u}_n$, which have the form

$$\hat{u}_n = A\mathrm{e}^{-\mathrm{i}k_n x} + B\mathrm{e}^{-\mathrm{i}k_n(L-x)}, \quad k_n = \omega_n \sqrt{\frac{\rho}{E}} \tag{2}$$

This expression for $\hat{u}_n$ is the frequency-dependent rod element shape function. Observe that the wavenumber, k_n, depends on not only frequency, but also the material through which longitudinal waves are traveling. In the equations that follow, the subscript n is dropped, however still implied.

The coefficients A and B can be solved for in terms of the nodal displacements by applying the boundary conditions

$$\hat{u}(x = x_1, \omega) = \hat{u}_1 \tag{3}$$

$$\hat{u}(x = x_2, \omega) = \hat{u}_2 \tag{4}$$

$$\text{where } x_1 = 0, \quad x_2 = L \tag{5}$$

Consequently,

$$\begin{bmatrix} A \\ B \end{bmatrix} = \frac{1}{1 - \mathrm{e}^{-\mathrm{i}2kL}} \begin{bmatrix} 1 & -\mathrm{e}^{-\mathrm{i}kL} \\ -\mathrm{e}^{-\mathrm{i}kL} & 1 \end{bmatrix} \begin{bmatrix} \hat{u}_1 \\ \hat{u}_2 \end{bmatrix} \tag{6}$$

The nodal forces for a rod element are found in terms of the spectral element stiffness matrix by taking the result from (6), placing it in (2), and forming expressions for the rod element axial loads:

$$\hat{F}_i = n_i E A \frac{\mathrm{d}\hat{u}}{\mathrm{d}x}\bigg|_{x=x_i} \quad \text{where } n_i = \begin{cases} -1 & \text{for } i = 1 \\ 1 & \text{for } i = 2 \end{cases} \tag{7}$$

resulting in

$$\hat{F}_1 = -EA \left. \frac{\mathrm{d}\hat{u}}{\mathrm{d}x} \right|_{x=x_1} \tag{8}$$

$$\hat{F}_2 = EA \left. \frac{\mathrm{d}\hat{u}}{\mathrm{d}x} \right|_{x=x_2} \tag{9}$$

or, in matrix form,

$$\begin{bmatrix} \hat{F}_1 \\ \hat{F}_2 \end{bmatrix} = EA \frac{\mathrm{i}k}{1 - \mathrm{e}^{-\mathrm{i}2kL}} \begin{bmatrix} 1 + \mathrm{e}^{-\mathrm{i}2kL} & -2\mathrm{e}^{-\mathrm{i}kL} \\ -2\mathrm{e}^{-\mathrm{i}kL} & 1 + \mathrm{e}^{-\mathrm{i}2kL} \end{bmatrix} \begin{bmatrix} \hat{u}_1 \\ \hat{u}_2 \end{bmatrix} \tag{10}$$

$$\boxed{\hat{\mathbf{F}}_{\mathrm{r}} = \hat{\mathbf{K}}_{\mathrm{r}} \hat{\mathbf{d}}_{\mathrm{r}}} \tag{11}$$

2.2. Beam element formulation

The development of the spectral beam element is similar to that of the rod element. Bending degrees of freedom allow for the transmission of flexural or transverse waves through the beam element rather than the longitudinal waves propagating in a rod element. Hence, the space–time solution for the transverse displacement of a point on the beam can be represented by

$$v(x, t) = \sum_n \hat{v}_n(x, \omega_n) \mathrm{e}^{\mathrm{i}\omega_n t} \tag{12}$$

The frequency-dependent spectral displacements and wavenumber for the beam element have the form

$$\hat{v}_n = C\mathrm{e}^{-\mathrm{i}k_n x} + D\mathrm{e}^{-k_n x} + F\mathrm{e}^{-\mathrm{i}k_n(L-x)} + G\mathrm{e}^{-k_n(L-x)}, \quad k_n = \sqrt{\omega_n} \left[\frac{\rho A}{EI} \right]^{1/4} \tag{13}$$

Based on this displacement function, the rotation, $\hat{\phi}_n$, at each end of the beam can be found by taking the derivative of (13) with respect to x:

$$\hat{\phi}_n = \frac{\mathrm{d}\hat{v}_n}{\mathrm{d}x} \tag{14}$$

Applying the known boundary conditions to the element allows for the solution of the coefficients C, D, F, and G:

$$\hat{v}(x = x_1, \omega) = \hat{v}_1 \tag{15}$$

$$\hat{\phi}(x = x_1, \omega) = \hat{\phi}_1 \tag{16}$$

$$\hat{v}(x = x_2, \omega) = \hat{v}_2 \tag{17}$$

$$\hat{\phi}(x = x_2, \omega) = \hat{\phi}_2 \tag{18}$$

Consequently,

$$
\begin{bmatrix} C \\ D \\ F \\ G \end{bmatrix} = \hat{\mathbf{Q}} \begin{bmatrix} \hat{v}_1 \\ \hat{\phi}_1 \\ \hat{v}_2 \\ \hat{\phi}_2 \end{bmatrix} \tag{19}
$$

Matrix $\hat{\mathbf{Q}}$ is not given here for the sake of brevity, but is easily obtained using symbolical computation software. The beam nodal loads are then found, in terms of the spectral stiffness matrix, by substituting the coefficients C, D, F, and G back into (13) and differentiating the resulting displacement function to form the moment and shear force at each node:

$$
\hat{V}_i = n_i E I \frac{\mathrm{d}^3 \hat{v}}{\mathrm{d}x^3} \bigg|_{x=x_i} \tag{20}
$$

$$
\hat{M}_i = -n_i E I \frac{\mathrm{d}^2 \hat{v}}{\mathrm{d}x^2} \bigg|_{x=x_i} \tag{21}
$$

In matrix form,

$$
\boxed{\hat{\mathbf{F}}_\mathrm{b} = \hat{\mathbf{K}}_\mathrm{b} \hat{\mathbf{d}}_\mathrm{b}} \tag{22}
$$

where

$$
\hat{\mathbf{F}}_\mathrm{b} = \begin{bmatrix} \hat{V}_1 \\ \hat{M}_1 \\ \hat{V}_2 \\ \hat{M}_2 \end{bmatrix} \quad \text{and} \quad \hat{\mathbf{d}}_\mathrm{b} = \begin{bmatrix} \hat{v}_1 \\ \hat{\phi}_1 \\ \hat{v}_2 \\ \hat{\phi}_2 \end{bmatrix} \tag{23}
$$

2.3. Frame element formulation and implementation

The spectral frame finite element and conventional frame finite element are formulated in a similar manner. The 2×2 matrix, $\hat{\mathbf{K}}_\mathrm{r}$, of the spectral rod element and the 4×4 matrix, $\hat{\mathbf{K}}_\mathrm{b}$, of the spectral beam element can be combined to describe a two-dimensional spectral frame element with three (i.e. longitudinal, transverse, and rotational) degrees of freedom per node. The resulting dynamic stiffness matrix, $\hat{\mathbf{K}}_\mathrm{f}$, is 6×6 and, in terms of assembly on a global level, implemented in precisely the same way as in the conventional formulation.

Major differences are that the global stiffness matrix is complex and frequency dependent, and wave propagation effects are included eliminating the need for a separate mass matrix. The step-by-step time integration problem from the conventional formulation now becomes a step-by-step frequency problem, and instead of solving a differential equation in time a pseudo-static equation in frequency must be solved. Additionally, element subdivisions of structural members for proper mass and stiffness distribution are no longer required, reducing problem size. Single elements

between structural discontinuities can be utilized. Therefore, due to the ability to accurately and efficiently model wave propagation, this computational approach serves as an appropriate tool for straightforward modal analysis in the middle frequency range.

2.4. Spectral finite element method—numerical implementation

In the following sections, the spectral finite element method was numerically implemented as a computational code in MATLAB. The initial step in the numerical scheme is to define the geometry and material parameters for the structure of interest. Since the dynamic stiffness matrix and nodal load vector for each element are frequency dependent, they are next computed within a predefined loop that steps over a set number of frequencies. Additionally, within this computational loop, the global dynamic stiffness matrix and nodal load vector are assembled. The application of boundary conditions then follows to condense the system, and the spectral displacements at the frequency of interest are computed by solving the equilibrium equations $\hat{\mathbf{d}} = \hat{\mathbf{K}}^{-1}\hat{\mathbf{F}}$ for the structure. The spectral displacements are then stored to disk and the computational loop is stepped through at the next frequency increment.

3. COMPLIANT MECHANISM UNIT CELL AND STRUCTURE—ANALYSIS AND DESIGN

Earlier research [18] has demonstrated the suitability of using a local level 'unit cell' analysis in predicting the global response of periodic truss structures like those shown in Figures 2 and 3. In evaluating the vibro-acoustic behavior of such structures, the output (i.e. top layer) root-mean-square (RMS) normal velocity traditionally has been of interest since sound in a fluid domain is linked to pressure level variation and hence to the energy of motion or normal velocity of a radiating object [17]. This section builds upon prior work by establishing that compliant mechanisms can be used effectively at a local unit cell level to attenuate broadband vibro-acoustic response on a global level. Specifically, the unit cell can be thought of as a framework into which a compliant mechanism topology is placed in order to employ local level deformations and reduce the output normal velocity of a structure.
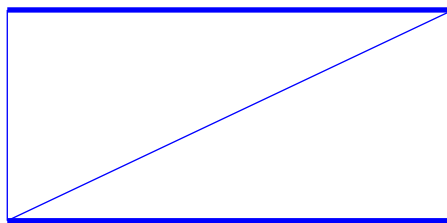

Figure 2. Square core unit cell.

Figure 3. Periodic square core structure.

3.1. Compliant mechanism unit cell and structure—concept and definitions

Generally, a compliant mechanism topology with a large mechanical advantage is sought. Let $\mathbf{F}_{in}$ and $\mathbf{F}_{out}$ be the respective input and output force vectors; similarly $\mathbf{v}_{in}$ and $\mathbf{v}_{out}$ denote the velocity vectors of the points of force input and output, respectively. Then, assuming that the velocity and force vectors are parallel, and assuming conservation of power we have, according to [23], that

$$\mathrm{MA} = \frac{F_{out}}{F_{in}} = \frac{v_{in}}{v_{out}} \tag{24}$$

where the scalar quantities denote the corresponding magnitudes and MA is the mechanical advantage. Thus, for a given input speed, v_{in}, the output speed, v_{out}, can be reduced by seeking a mechanism topology with a large mechanical advantage.

A prototypical rigid link 4-bar mechanism is shown in Figure 4 with a compliant mechanism unit cell realization of the rigid link mechanism given in Figure 5. This mechanism topology was first examined for micro-electro-mechanical (MEM) device applications [24], and was selected for investigation in this work since its general behavior is well characterized, making it a suitable benchmark. This mechanism is considered part of a class of mechanisms known as 'inversors', where the input and output move in opposite directions. As a point of departure, while MEM applications have applied actuators in generating mechanism motion, the following work exercises
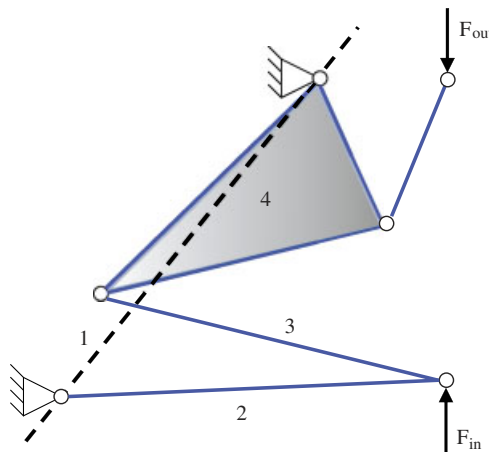

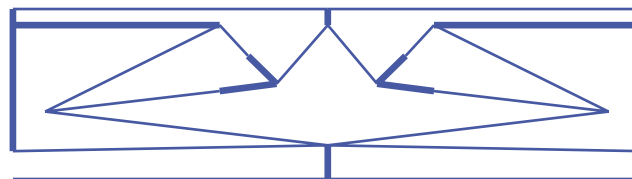Figure 4. Rigid link 4-bar mechanism diagram (numbers denote links).
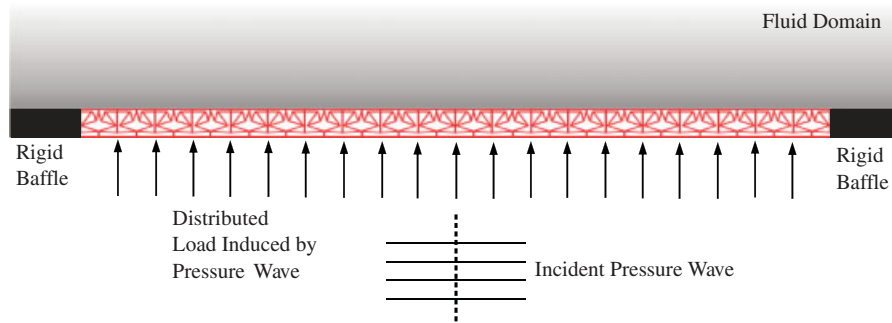

Figure 5. Compliant mechanism unit cell model.

Figure 6. Periodic compliant mechanism structure.

the notion of vibro-acoustically induced response. Thus, vibration isolation is accomplished pas-sively *via* a number of embedded compliant mechanisms within a structure rather than actively. Moreover, the implementation of this mechanism is varied slightly from [24] since it is used as a stroke reducer, instead of a stroke amplifier.

The conceptual model of a full compliant mechanism structure is shown in Figure 6, comprising an assembly of 20 unit cells. The structure is fixed to a rigid baffle at both ends and is subjected to a distributed load induced by an incident pressure wave.

In the compliant mechanism unit cell model given in Figure 7, frame elements 1, 2, 8, 10, 12, 14, 15 and their symmetric counterparts are shown with thicker lines. This implies that these elements are modeled as stiffer beams than the rest of the unit cell, although they still technically have compliance. The purpose of making elements 1, 2, and 8 stiffer is that these elements represent the *ground* for the mechanism. Elements 10 and 12 provide reinforcement for link 4 as shown in the rigid link mechanism diagram. Lastly, the input to the mechanism, element 14, and its output counterpart, element 15, are also modeled with stiffer beams since they are *transmission* members and minimal deflection is desired. The remaining elements in the unit cell are considered *core* members in which greater flexibility is desired.

In terms of element connectivity within the unit cell, the *ground* elements are connected to the output/top side of the structure. The mechanism input is then connected through a single element to the bottom layer, allowing transverse waves generated by the incident pressure field to propagate through elements 3 and 20. As the wavelength of vibration, λ, approaches the length scale of the unit cell (Figure 7), these transverse waves actuate the compliant mechanism evoking mechanical advantage and reducing the top layer normal velocity of the structure.

While the unit cell element connectivity affects the frequency at which response attenuation starts, the width, w in Figure 7, of the *core* elements in the unit cell dictates the attenuation zone cutoff. The natural frequency of the mechanism is linked to this sizing, with increased stiffness leading to a greater cutoff frequency. The frequency response function (FRF) amplitude and phase of the mechanism output displacement relative to input displacement are defined to illustrate this relationship:

$$\text{Amplitude} = \left| \frac{\hat{v}_{13} - \hat{v}_4}{\hat{v}_{10} - \hat{v}_2} \right|, \quad \text{Phase} = \frac{180}{\pi} [\angle(\hat{v}_{13} - \hat{v}_4) - \angle(\hat{v}_{10} - \hat{v}_2)] \tag{25}$$
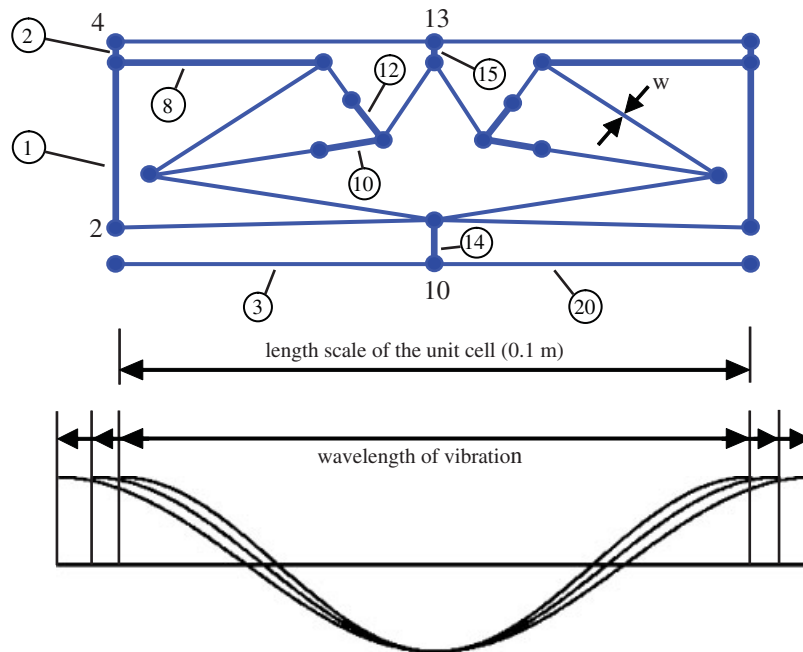
Figure 7. Compliant mechanism unit cell model (numbers that are circled denote elements; numbers that are not circled denote nodes).

where the output is taken as the transverse spectral displacement of node 13 relative to node 4, while the input is taken as the transverse spectral displacement of node 10 relative to node 2. Nodes 4 and 2 are selected since they are part of the *ground* of the mechanism.

Lastly, to predict the frequency at which attenuation begins, a straightforward wavenumber analysis is used. The wavenumber for transverse waves in a beam element, from (13), and its relationship to wavelength are combined to yield the following wavenumber–frequency equation:

$$k = \sqrt{\omega}\left[\frac{\rho A}{EI}\right]^{1/4} \quad \text{and} \quad \lambda = \frac{2\pi}{k} \Rightarrow \omega = \left(\frac{2\pi}{\lambda}\right)^2 \sqrt{\frac{EI}{\rho A}} \tag{26}$$

where ρ, E, A, and I are the physical parameters of the bottom layer elements.

3.2. Compliant mechanism unit cell and structure—analysis

Prior to solving for the response of the unit cell or structure, the spectral load vector equivalent to the incident pressure for each element, e, must be formulated. From [18], the element spectral load vector equivalent can be expressed as

$$\hat{\mathbf{f}}^{e}(\hat{\mathbf{w}}_{b}, \omega) = \int_{0}^{L^{e}} \hat{\mathbf{w}}_{b}(x, \omega) p_{in} \, dx \tag{27}$$

where $\hat{\mathbf{w}}_{b}$ is the spectral weighting function for the beam element, L^{e} is the length of the beam element, and p_{in} is the normally incident pressure wave amplitude.

Symmetric boundary conditions, representative of those imposed on a unit cell when assembled into the full structure, are enforced in the unit cell analysis. Rotational degrees of freedom of the nodes on the left and right edges of the unit cell are constrained, with all the remaining degrees of freedom unconstrained. For the full structure, only the degrees of freedom of nodes interfacing with the rigid baffles are constrained.

Following [17], the response is computed in terms of the top layer nodal RMS transverse velocity given in decibels by

$$v_{\text{RMS}} = 20 \log_{10} \left[\frac{\omega}{v_{\text{ref}}} \left[\frac{1}{N} \sum_{j=1}^{N} |\hat{v}_{\text{t}}|_j^2 \right]^{1/2} \right] \tag{28}$$

where ω is the frequency of interest, v_{ref} is a reference velocity, $\hat{v}_{\text{t}}$ is the transverse spectral displacement of the jth node of interest, and N is the number of top layer nodes.

While the top layer RMS normal velocity of the structure is related to the energy of motion, another measure of the reduction of sound radiated by the compliant mechanism structure is the far-field sound pressure level (SPL). A numerical approximation to the SPL for a baffled rectangular radiator was suggested in [18]. Specifically, the pressure level distribution in the acoustic fluid domain above the structure is evaluated numerically using results from the spectral finite element analysis by way of the Fourier transform solution to the Helmholtz equation:

$$p_{\text{t}}(x, y, \omega) \cong \frac{-\mathrm{i}\rho_{\text{f}}\omega^2}{2\pi} \sum_{-m}^{m} \hat{v}_{\text{t}}(m\Delta\gamma_x, \omega) \frac{\mathrm{e}^{\mathrm{i}y\sqrt{k^2 - (m\Delta\gamma_x)^2}}}{\sqrt{k^2 - (m\Delta\gamma_x)^2}} \mathrm{e}^{\mathrm{i}m\Delta\gamma_x x} \Delta\gamma_x \tag{29}$$

This equation is the numerical form of the integral representation of the pressure at a specific frequency, ω, of interest. The integral is approximated as a summation over m number of finite, $\Delta\gamma_x$, steps, where γ_x is the usual transform parameter, according to [25]. In (29) ρ_{f} is the density of the fluid and $k = \omega/c_{\text{a}}$ is the acoustic wavenumber, where c_{a} is the speed of sound in the fluid. The form of the numerically evaluated transverse displacement transform, $\hat{v}_{\text{t}}(m\Delta\gamma_x, \omega)$, can be found in [18].

In the next section, the RMS normal velocity response and SPL of the compliant mechanism unit cell and structure are compared, respectively, with that of a square core unit cell and structure. The square core structure represents an analysis control for comparison. In all analyses the forcing function and boundary conditions are implemented in the manner described above.

3.3. Compliant mechanism unit cell and structure—results

For this work, both the compliant mechanism structure and square core structure are assumed to be made of aluminum with a material Young's modulus $E = 7.1 \times 10^{10} \, \text{N/m}^2$ and density $\rho = 2700 \, \text{kg/m}^3$. As is typical of such structures, hysteretic material damping is introduced to account for inherent energy loss. A complex modulus, $E^* = E(1 + \mathrm{i}\eta)$, is utilized, where the loss factor $\eta = 0.01$. This value is slightly high relative to typical values reported for aluminum [26], but consistent with prior research [17, 18]. However, the effect of using a slightly higher loss factor has been explored, with the result that resonant peaks are damped whereas the fundamental frequency response of general interest is basically unchanged.

Unit cell dimensions of 0.1 m by 0.05 m, and structure dimensions of 2 m by 0.05 m, are used. This sizing of the unit cell leads to a compliant mechanism mechanical advantage of 8.3. The

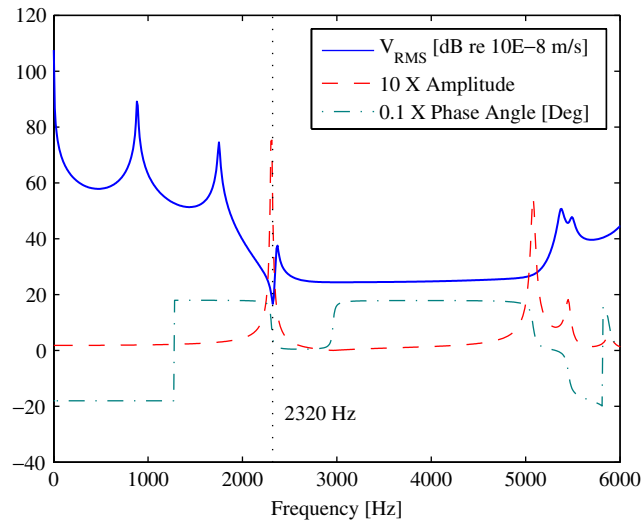480 E. M. DEDE AND G. M. HULBERT

Figure 8. Compliant mechanism unit cell FRF.

width of *core* elements for the compliant mechanism unit cell is taken as 2.5 mm while stiffer members (e.g. *ground*, *transmission*, etc.) are given a width of 5.0 mm. These initial widths were chosen since they are comparable to those used in the square core structure, which has a *core* member thickness of 2.5 mm and a facesheet thickness of 5.0 mm.

For each structure, the incident pressure field amplitude in (27) is $p_{in} = 1 \, \text{N/m}^2$. In computing the RMS transverse velocity of each structure, a reference velocity in (28), $v_{ref} = 10^{-8} \, \text{m/s}$, is used. For calculation of the far-field SPL, (29) is summed from $m = -100$ to 100 and each structure is assumed to be in air with $\rho_f = 1.2 \, \text{kg/m}^3$ and $c_a = 343 \, \text{m/s}$.

The frequency range of interest for this study is 0–6000 Hz, evaluated at 10 Hz frequency steps. The unit cell FRF is given in Figure 8, where the amplitude and phase are scaled for visual clarity by factors of 10 and 1/10, respectively. Below 2 kHz, two prominent peaks in response are visible at 880 and 1780 Hz, representing resonances of the unit cell at frequencies below the attenuation starting frequency. Substituting the physical parameters of elements 3 and 20 into (26), along with $\lambda = 0.1 \, \text{m}$ (i.e. the length of the unit cell), gives an attenuation starting frequency of 2320 Hz, accurately predicting the response shown in Figure 8. Moreover, the FRF illustrates that within the attenuation zone the compliant mechanism exhibits non-resonant (i.e. small amplitude), out-of-phase 'inversor' behavior. At the first cutoff frequency of 5300 Hz, resonance is characterized by a large amplitude and in-phase behavior.

The top layer RMS transverse velocity of the compliant mechanism unit cell and structure are plotted in comparison with the square core unit cell and structure, respectively, in Figures 9 and 10. The square core unit cell response exhibits four main peaks at 1120, 2600, 3870, and 5900 Hz. These peaks are also evident in the response of the square core structure, where the resonance at 3870 Hz is dominant above 2 kHz. For the compliant mechanism structure, the resonances at 880 and 1780 Hz, visible in the unit cell response, are again present. Between 2320 and 5300 Hz significant broadband attenuation is apparent, most notably at 3870 Hz, where a reduction upwards of 40 dB is seen relative to the square core structure.
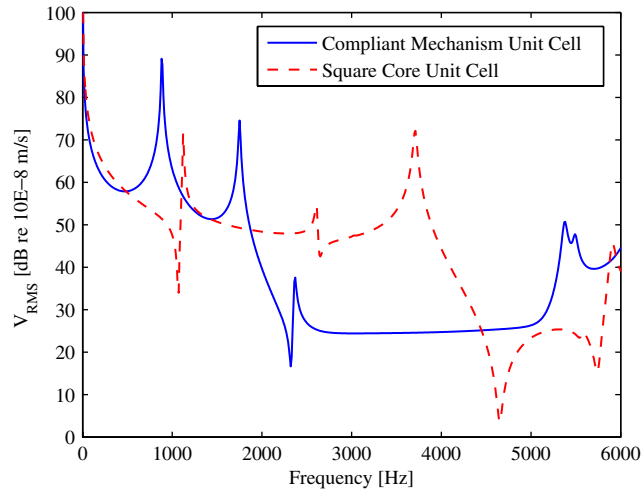
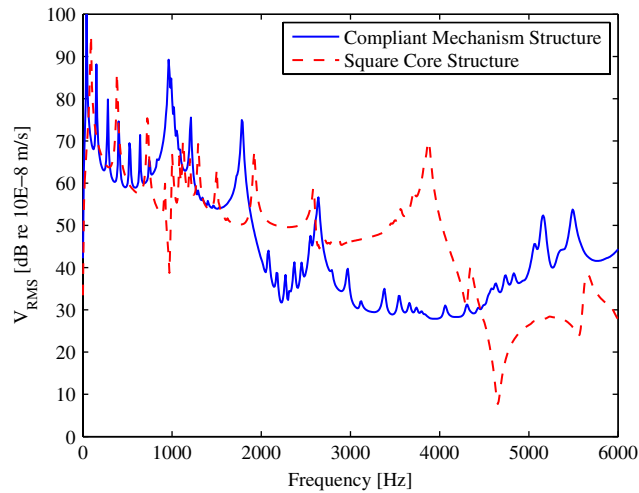Figure 9. Top layer RMS velocity comparison for unit cell.

Figure 10. Top layer RMS velocity comparison for structure.

To supplement the FRF and RMS transverse velocity results, the deformed shapes of the unit cell can also be plotted along with element energetics to gain additional knowledge of the behavior of the structure. The total energy of each element is evaluated using the 6×6 spectral stiffness matrix, $\hat{\mathbf{K}}_f$, for a given frame element once the 6×1 spectral nodal displacement vector, $\hat{\mathbf{d}}_f$,
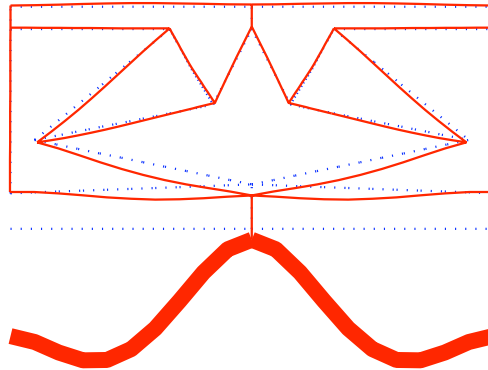
Figure 11. Compliant mechanism unit cell deformed shape and energy distribution at 3500 Hz (dotted lines denote undeformed configuration; continuous lines denote deformed configuration).
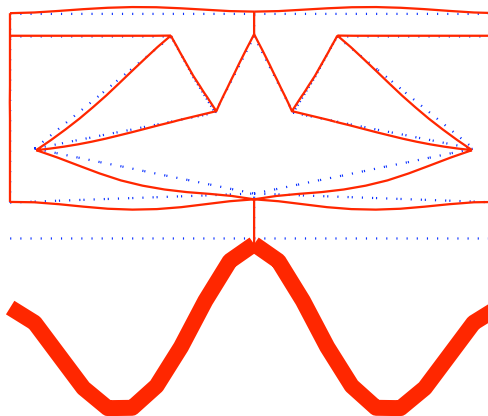

Figure 12. Compliant mechanism unit cell deformed shape and energy distribution at 4500 Hz (dotted lines denote undeformed configuration; continuous lines denote deformed configuration).

for that element has been computed.

$$E^{\mathrm{e}} = |\tfrac{1}{2}\hat{\mathbf{d}}_{\mathrm{f}}^{\mathrm{T}}\hat{\mathbf{K}}_{\mathrm{f}}\hat{\mathbf{d}}_{\mathrm{f}}| \tag{30}$$

The deformed shape and total energy at several frequencies provide fundamental insight into the compliant mechanism unit cell performance; see Figures 11–14. Thicker continuous lines denote greater energy content. Within the attenuation zone (Figures 11 and 12) energy isolation is evident, corresponding to the propagation of a transverse wave in the bottom layer and the mechanism acting as an 'inversor.' At the first mechanism resonance (Figure 13) in-phase behavior is observed. Outside the attenuation zone (Figure 14) energy flows into the core and top layer.
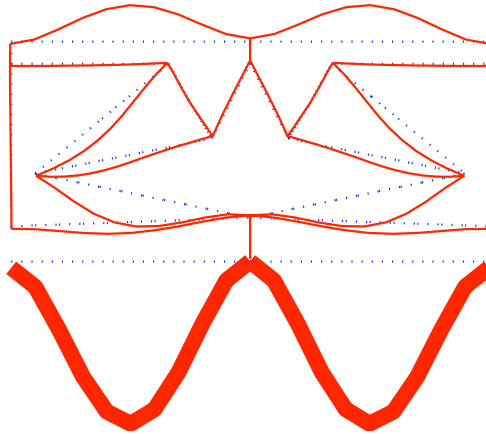
Figure 13. Compliant mechanism unit cell deformed shape and energy distribution at 5220 Hz (dotted lines denote undeformed configuration; continuous lines denote deformed configuration).
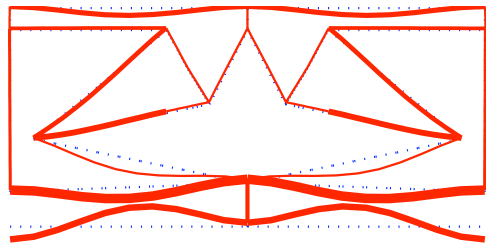

Figure 14. Compliant mechanism unit cell deformed shape and energy distribution at ∼6000 Hz (dotted lines denote undeformed configuration; continuous lines denote deformed configuration).

A comparison is made of the far-field SPL in the fluid region above both structures at 1780 and 3870 Hz. Figures 15 and 16, respectively, illustrate that the compliant mechanism core structure indeed produces a higher SPL at 1780 Hz, as expected based on the RMS velocity response. Note that the structure top layer is located between −1 m and +1 m along the bottom horizontal axis of these figures and that the SPL radiation patterns are dependent upon the unique deformation of each structure. Furthermore, a reduced SPL of nearly 40 dB at 3870 Hz, within the attenuation zone, is seen in Figures 17 and 18. These results represent a significant reduction in transmitted sound.

Moving to a global view, deformed configurations of the compliant mechanism structure are given in Figures 19–21 at frequencies of 40, 150, and 3000 Hz, respectively. It is evident that as frequency increases, the deformed shape transitions from global to local. The local deformation at 3000 Hz illustrates the propagation of a transverse wave traveling through the bottom layer of the structure.
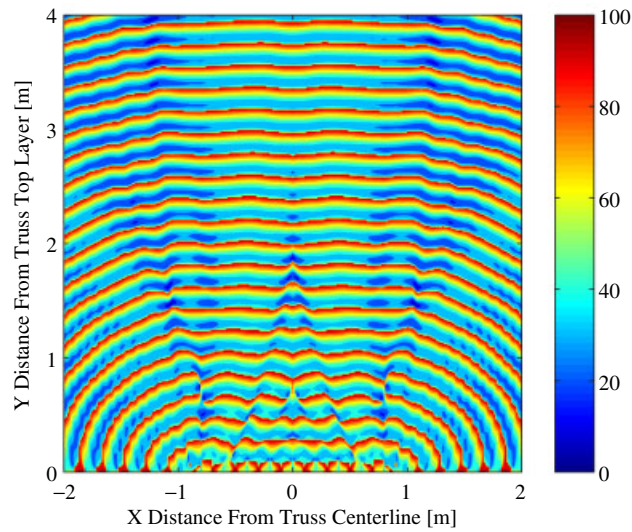
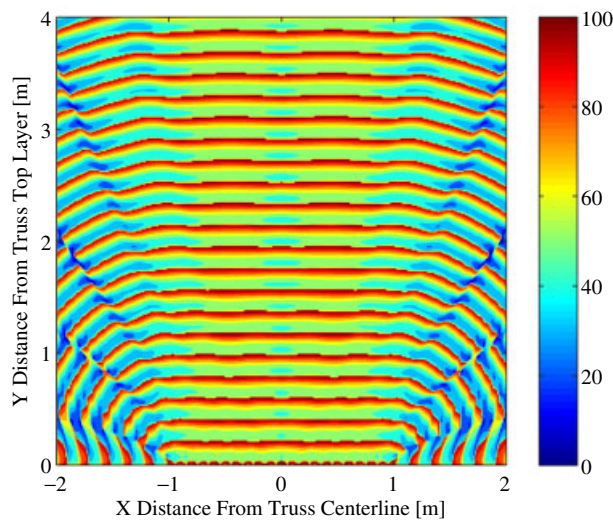Figure 15. Square core structure SPL at 1780 Hz—units: dB re 20E−6 Pa.

Figure 16. Compliant mechanism core structure SPL at 1780 Hz—units: dB re 20E−6 Pa.

4. GENETIC ALGORITHM OPTIMIZATION

Having described the compliant mechanism unit cell design and analysis concept, the next logical step in formulating a unified methodology is to optimize these structures for a desired response in a known frequency range. As discussed in [20], the efficiency of a genetic algorithm comes
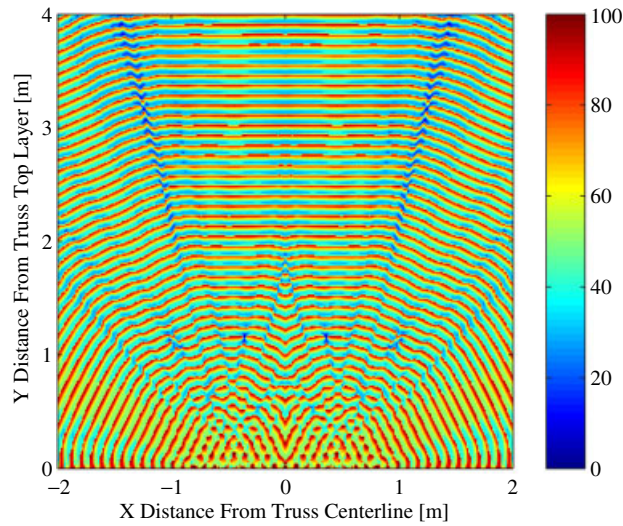
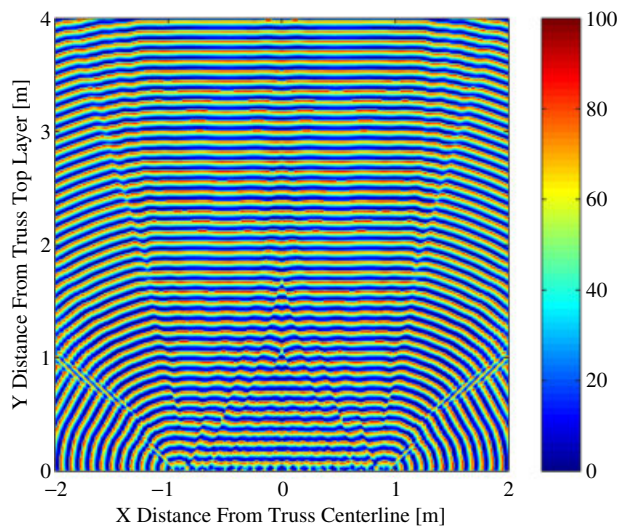Figure 17. Square core structure SPL at 3870 Hz—units: dB re 20E−6 Pa.

Figure 18. Compliant mechanism core structure SPL at 3870 Hz—units: dB re 20E−6 Pa.

from the fact that while randomized, it uses historical information based on design fitness to search new spaces. Additionally, a genetic algorithm can handle noisy data in a global search that does not examine only local maxima and minima as calculus-based methods do. Thus, genetic algorithms have a notable advantage in optimizing truss-like structures that have a large number of non-linear, inter-related variables, which produce a broadband frequency response with many
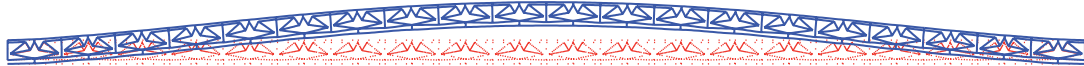
Figure 19. Deformed shape of compliant mechanism structure at 40 Hz (dotted lines denote undeformed configuration; continuous lines denote deformed configuration).

Figure 20. Deformed shape of compliant mechanism structure at 150 Hz (dotted lines denote undeformed configuration; continuous lines denote deformed configuration).
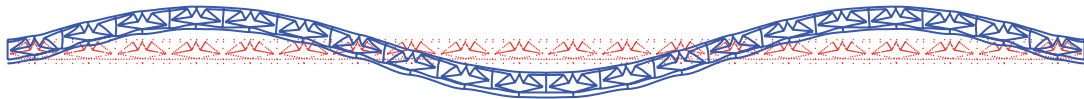

Figure 21. Deformed shape of compliant mechanism structure at 3000 Hz (dotted lines denote undeformed configuration; continuous lines denote deformed configuration).

resonant peaks [21]. Accordingly, a genetic algorithm is chosen over a calculus-based method and is coupled to the aforementioned spectral finite element analysis. The genetic algorithm used in this study has the standard operations, according to [20], found in most applications: (1) selection of candidate individuals from an initial population according to their fitness value (FV); (2) crossover, where portions of two individuals are combined to create a new individual; (3) mutation, where small, random changes are introduced. Additionally, an elitist survival strategy is implemented to ensure that the fittest individual from a given population survives in the next generation [21].

4.1. Genetic algorithm optimization—analysis

It is appropriate to define an objective in terms of 'response tuning.' As mentioned in Section 3.1, changing the thickness of various beam widths within the unit cell alters the attenuation zone breadth (due to modification of the mechanism stiffness and consequently natural frequencies). Hence, the objective for this model is to use a genetic algorithm to optimize the size of various beams in the unit cell and decrease the response over an extended frequency range. More specifically, the objective function is to minimize the following fitness value:

$$\min \text{FV} = \sum_n v_{\text{RMS}} \tag{31}$$

where the RMS velocity, v_{RMS}, is summed over the number of frequencies, n, spanning a frequency interval.

For the size optimization analysis a total of nine element width variables are used, one for each of the following elements: 4–7 and 9–13 (see Figure 22). Symmetry is enforced about the
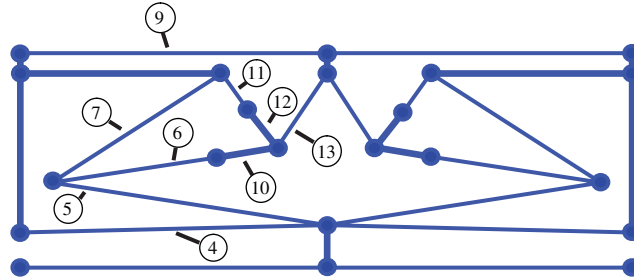
Figure 22. Compliant mechanism unit cell model (numbers that are circled denote elements).
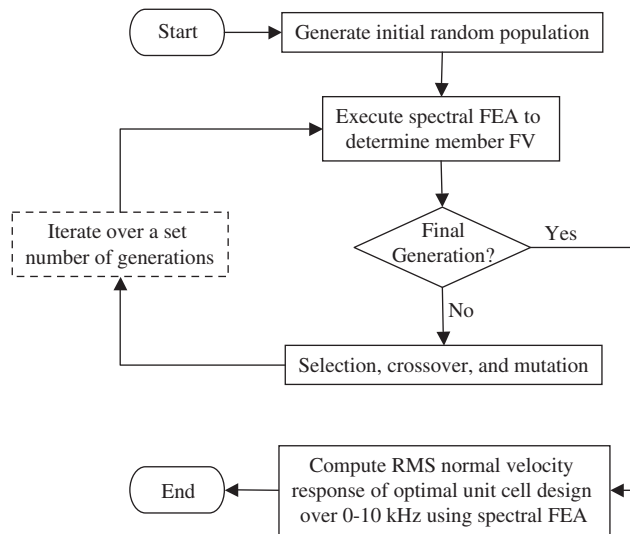

Figure 23. Flowchart of computations for unit cell genetic algorithm size optimization.

centerline of the unit cell. The elements chosen for size optimization include the mechanism *core* and top layer elements, but not the *ground*, *transmission*, or bottom layer elements. The latter groups, not selected for size optimization, are considered paramount to the behavior established in Figure 8. For example, the bottom layer element width should not be modified since that will change the frequency at which the attenuation zone begins, according to (26).

4.2. Genetic algorithm optimization—numerical implementation

A flowchart of the unit cell genetic algorithm size optimization routine is shown in Figure 23. The optimization algorithm was numerically implemented in MATLAB in tandem with the spectral finite element analysis computational code. The numerical procedure requires the generation of an initial random population after which spectral finite element analyses are conducted to compute the fitness value for each individual over the specified frequency range. From there the optimizer performs selection, crossover, and mutation and the fitness values of the new population members

are computed using the spectral finite element analysis. This procedure is iterated over a set number of generations and the final size optimized design is obtained.

4.3. Genetic algorithm optimization—results

The width of each element was allowed to vary $+75\%/-50\%$ from an initial value of 2.5 mm. An 18-bit binary encoding was used in the genetic algorithm for the nine variables. A population size of 10 was iterated over four generations. Given the range of FVs for the members of the population, individuals within the top 80% were selected and copied into a mating pool with fitter members more represented. Among those surviving individuals, 80% of them were allowed to crossover (i.e. breed), after which a mutation rate of 1% was applied.

The compliant mechanism unit cell was optimized to minimize the fitness value over the frequency interval of 5000–7000 Hz at frequency steps of 10 Hz with $n = 200$ in (31). In particular, response peaks at 5400 and 6200 Hz were targeted for reduction. The RMS transverse velocity of the optimized unit cell response was then computed over the entire 0 Hz–10 kHz range at 10 Hz frequency steps and is shown in Figure 24. An average reduction of 9 dB was achieved over the 5000–7000 Hz frequency range with a significant reduction of 25 dB at 5400 Hz and 30 dB at 6200 Hz. Comparing the initial and optimized responses, it is clear that the unit cell resonances have been shifted to the right across the majority of the 10 kHz range, implying a somewhat stiffer structure.

The final width of each size optimized element is given in Table I and the initial and optimized unit cell structures are shown in Figures 25 and 26, respectively. Element width is represented by varying line thickness. The thicker elements in the optimized structure are consistent with the notion of it being stiffer, leading to a shift of the unit cell resonances toward higher frequencies. These optimization results are quite promising given that only four generations were evaluated, each with a population size of only 10 individuals.
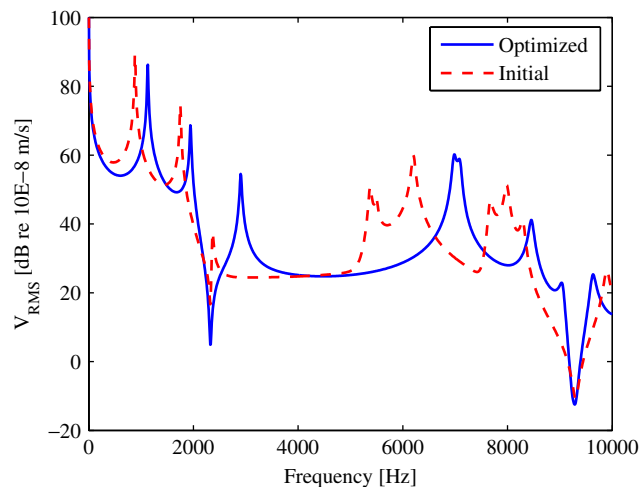

Figure 24. RMS velocity of compliant mechanism unit cell.

Table I. Initial and optimized width of elements in the compliant mechanism unit cell.

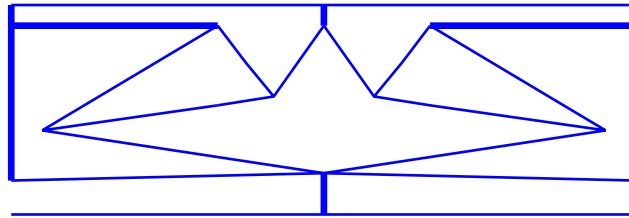| Element number	Initial width (mm)	Optimized width (mm)
4	2.5	3.3
5	2.5	3.3
6	2.5	3.3
7	2.5	4.3
9	2.5	4.3
10	2.5	2.3
11	2.5	3.3
12	2.5	4.3
13	2.5	4.3

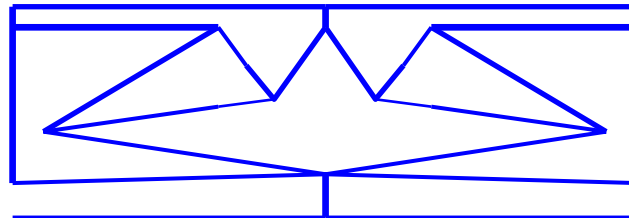Figure 25. Initial compliant mechanism unit cell.

Figure 26. Optimized compliant mechanism unit cell.

5. CONCLUSIONS

In this study, an analysis, design, and optimization methodology was introduced for structures with integral compliant mechanisms for middle frequency structural-borne noise attenuation. The computational utility of the spectral finite element method was discussed. Several concepts and analysis tools were outlined for initial unit cell sizing and structure design, including (1) amplification principles for topology selection, (2) the compliant mechanism FRF, (3) the wavenumber–frequency analysis, and (4) the deformed shape/energy distribution analysis. A genetic algorithm optimization routine was shown to provide control in adjusting the attenuation frequency range. Results of a specific computational example verified that, using this assemblage of numerical methods, structures with enhanced vibro-acoustic properties can be realized.

This work brings together several stand-alone research areas including structural dynamics, compliant mechanism design, spectral finite element computational analysis, and structural optimization. This study suggests that this approach to the problem of vibration-induced noise, implemented during the *design stage* of a vehicle or structure, can be added to the list of existing solutions. Moreover, the fact that these structures have possible load bearing capability also suggests that they can fulfill multi-functional objectives.

Further work is being performed on the analysis, design, manufacturing, and testing of a compliant mechanism prototype structure for model validation. Future computational research will explore an enhanced genetic algorithm optimization routine to include shape and topology optimization. Additional research is also being carried out in conjunction with the design of 3-D truss-like structures for acoustic attenuation panels and other unique applications.

APPENDIX: NOMENCLATURE

List of symbols

n	number of frequencies
m	number of transform parameter steps
i	element nodal index
j	structure top layer nodal index
N	number of top layer nodes
ρ, ρ_f	material density
E	Young's modulus
η	loss factor
A	element cross-sectional area
L, L^e	length of element
w	width of element
I	element area moment of inertia
$F_i, \hat{F}_i$	longitudinal force and longitudinal spectral force, respectively
$u_i, \hat{u}_i$	longitudinal displacement and longitudinal spectral displacement, respectively
$V_i, \hat{V}_i$	transverse force and transverse spectral force, respectively
$M_i, \hat{M}_i$	moment and spectral moment, respectively
$v_i, \hat{v}_i$	transverse displacement and transverse spectral displacement, respectively
θ_i	rotation
$\hat{\phi}_i$	spectral rotation
ω, ω_n	frequency
k, k_n	wavenumber
$\hat{\mathbf{F}}_r, \hat{\mathbf{F}}_b$	rod and beam element spectral force vectors, respectively
$\hat{\mathbf{d}}_r, \hat{\mathbf{d}}_b, \hat{\mathbf{d}}_f$	rod, beam, and frame element spectral displacement vectors, respectively
$\hat{\mathbf{K}}_r, \hat{\mathbf{K}}_b, \hat{\mathbf{K}}_f$	rod, beam, and frame element spectral stiffness matrices, repectively
$\mathbf{F}_{in}, \mathbf{F}_{out}$	input and output force vectors, respectively
$\mathbf{v}_{in}, \mathbf{v}_{out}$	velocity vectors of points of force input and output, respectively
F_{in}, F_{out}	magnitude of input and output force vectors, respectively
v_{in}, v_{out}	input and output speeds, respectively

λ	wavelength of vibration
$\hat{\mathbf{f}}^e$	element spectral load vector equivalent to the incident pressure
$\hat{\mathbf{w}}_b$	spectral weighting function for the beam element
p_{in}	normally incident pressure wave amplitude
p_t	pressure in the fluid domain above the structure
v_{RMS}	RMS velocity
v_{ref}	reference velocity
$\hat{v}_t$	transverse spectral displacement of a top layer node
c_a	speed of sound in air
γ_x	transform parameter
$\Delta\gamma_x$	transform parameter step
E^e	total energy of element

Abbreviations

RMS	root mean square
MA	mechanical advantage
MEM	micro-electro-mechanical
FRF	frequency response function
SPL	sound pressure level
FV	fitness value

REFERENCES

1. Bhat WV. Flight test measurement of exterior turbulent boundary layer pressure fluctuations on Boeing model 737 airplane. *Journal of Sound and Vibration* 1971; **14**(4):439–457.
2. Bhat WV, Wilby JF. Interior noise radiated by an airplane fuselage subjected to turbulent boundary layer excitation and evaluation of noise reduction treatments. *Journal of Sound and Vibration* 1971; **18**(4):449–464.
3. Frampton D, Clark RL. Sound transmission through an aeroelastic plate into a cavity. *American Institute of Aeronautics and Astronautics Journal* 1997; **35**(7):1113–1118.
4. Science Magazine Page: Noisy Days Aboard the Space Station. From http://www.sciencemag.org/content/vol290/issue5500/r-samples.dtl (25 July 2006).
5. Military Audiology Association Page: Noise Protection Health Effects Reduction. From http://www.militaryaudiology.org/newsletter04/nopher.html (25 July 2006).
6. Nashif AD, Jones DIG, Henderson JP. *Vibration Damping*. Wiley: New York, 1985.
7. Preumont A. *Vibration Control of Active Structures*: *An Introduction*. Kluwer: Boston, 2002.
8. Brillouin L. *Wave Propagation in Periodic Structures*: *Electric Filters and Crystal Lattices* (1st edn). McGraw-Hill: New York, 1946.
9. Mead DJ, Parthan S. Free wave propagation in two-dimensional periodic plates. *Journal of Sound and Vibration* 1979; **64**(3):325–348.
10. Langley RS. The response of two-dimensional periodic structures to point harmonic forcing. *Journal of Sound and Vibration* 1996; **197**(4):447–469.
11. Fish J, Chen W, Nagai G. Non-local dispersive model for wave propagation in heterogeneous media: multi-dimensional case. *International Journal for Numerical Methods in Engineering* 2002; **54**(3):347–363.
12. Martinsson PG, Movchan AB. Vibrations of lattice structures and phononic band gaps. *Quarterly Journal of Mechanics and Applied Mathematics* 2003; **56**(1):45–64.
13. Ruzzene M, Scarpa F, Soranna F. Wave beaming effects in two-dimensional cellular structures. *Smart Materials and Structures* 2003; **12**(3):363–372.
14. Sigmund O, Jensen JS. Systematic design of phononic band-gap materials and structures by topology optimization. *Philosophical Transactions of the Royal Society A*: *Mathematical*, *Physical and Engineering Sciences* 2003; **361**(1806):1001–1019.

15. Hussein MI, Hulbert GM, Scott RA. Dispersive elastodynamics of 1D banded materials and structures: analysis. *Journal of Sound and Vibration* 2006; **289**(4–5):779–806.
16. Halkjaer S, Sigmund O, Jensen JS. Maximizing band gaps in plate structures. *Structural and Multidisciplinary Optimization* 2006; **32**(4):263–275.
17. El-Raheb M, Wagner P. Transmission of sound across a trusslike periodic panel: 2-D analysis. *The Journal of the Acoustical Society of America* 1997; **102**(4):2176–2183.
18. Ruzzene M. Vibration and sound radiation of sandwich beams with honeycomb truss core. *Journal of Sound and Vibration* 2004; **277**(4–5):741–763.
19. Doyle JF. *Wave Propagation in Structures*: *An FFT-Based Spectral Analysis Methodology*. Springer: New York, 1989.
20. Goldberg DE. *Genetic Algorithms in Search*, *Optimization*, *and Machine Learning*. Addison-Wesley: Reading, MA, 1989.
21. Keane AJ. Passive vibration control via unusual geometries: the application of genetic algorithm optimization to structural design. *Journal of Sound and Vibration* 1995; **185**(3):441–453.
22. Huebner KH, Thornton EA. *The Finite Element Method for Engineers* (2nd edn). Wiley: New York, 1982.
23. Erdman AG, Sandor GN, Kota S. *Mechanism Design*: *Analysis and Synthesis*. Prentice-Hall: Upper Saddle River, NJ, 2001.
24. Hetrick JA, Kota S. *Displacement Amplification Structure and Device*. U.S. Patent 6 557 436 B1, 2003.
25. Junger MC, Feit D. *Sound*, *Structures and their Interaction* (1st edn). MIT Press: Cambridge, MA, 1972.
26. Lazan BJ. *Damping of Materials and Members in Structural Mechanics* (1st edn). Pergamon Press: New York, 1968.